

End-to-End Analysis of Charge Stability Diagrams with Transformers

Rahul Marchand,^{1, a)} Lucas Schorling,^{1, a)} Cornelius Carlsson,¹ Jonas Schuff,^{2, 3} Barnaby van Straaten,⁴ Taylor L. Patti,⁵ Federico Fedele,¹ Joshua Ziegler,³ Parth Girdhar,¹ Pranav Vaidhyanathan,^{1, b)} and Natalia Ares^{1, c)}

¹⁾Department of Engineering Science, University of Oxford, Oxford OX1 3PJ, United Kingdom

²⁾Department of Materials, University of Oxford, Oxford OX1 3PH, United Kingdom

³⁾Intel Corporation, Technology Research Group, Hillsboro, OR 97124, USA

⁴⁾QuTech and Kavli Institute of Nanoscience, Delft University of Technology, P.O. Box 5046, Delft, 2600 GA, Delft, The Netherlands

⁵⁾NVIDIA Corporation, 2788 San Tomas Expressway, Santa Clara, 95051, CA, USA

(Dated: 22 August 2025)

Transformer models and end-to-end learning frameworks are rapidly revolutionizing the field of artificial intelligence. In this work, we apply object detection transformers to analyze charge stability diagrams in semiconductor quantum dot arrays, a key task for achieving scalability with spin-based quantum computing. Specifically, our model identifies triple points and their connectivity, which is crucial for virtual gate calibration, charge state initialization, drift correction, and pulse sequencing. We show that it surpasses Convolutional Neural Networks in performance on three different spin qubit architectures, all without the need for retraining. In contrast to existing approaches, our method significantly reduces complexity and runtime, while enhancing generalizability. The results highlight the potential of transformer-based end-to-end learning frameworks as a foundation for a scalable, device- and architecture-agnostic tool for control and tuning of quantum dot devices.

I. INTRODUCTION

Transformers and other attention-based models underpin the success of recent progress in artificial intelligence^{1–4}. Initially developed for natural language processing, transformers advance previous sequential-modeling approaches such as recurrent neural networks (RNN), and exhibit exceptional generalization capabilities along with high versatility^{5–8}. This enabled them to also outperform convolutional (CNN) on image-related tasks⁴ and to be rapidly adopted across a range of areas, including genomics⁹, robotics¹⁰, and more recently, quantum technologies¹¹.

In this work, we adapt a transformer-based model to analyze charge stability diagrams (CSD) of semiconductor quantum devices. Efficient feature extraction from CSDs is crucial for tuning and operating quantum dot arrays for quantum computing applications. Within quantum technologies, spin qubits based on gate-defined semiconductor quantum dots represent one of the leading platforms for realizing high-fidelity^{12,13}, hot ($\gtrsim 1$ K)^{14,15}, and scalable quantum processors^{16–18}. However, as the number of devices scales^{19,20}, the large number of parameters that must be finely optimized for each individual qubit presents a major bottleneck to scalability. In this context, automated control strategies, particularly those based on machine learning, are emerging as essential tools to enable reliable and efficient device operations^{21,22}.

Previous work relied on diverse machine learning techniques for automating tasks such as double quantum dot tuning^{23–26}, multi-parameter crosstalk compensation²⁷, spin-readout optimization²⁸, meta-learning qubit characteristics²⁹, and ultimately, the fully autonomous tuning of a spin qubit^{30,31}. However, previous approaches have typically relied on a variety of methods, including pre- and post-processing procedures, template matching, Hough transforms, (convolutional) neural network image or pixel classifiers, and combinations thereof^{32–39}. These solutions can be time-consuming and often result in pipelines with limited generalizability.

To address these challenges, we introduce TRACS (Transformers for Analyzing Charge Stability diagrams), a transformer-based model designed to process CSDs and extract their full graph structure. TRACS identifies the pattern of lines indicating charge transitions, and the points where these lines intersect (called triple points), enabling virtual gate calibration, charge state initialization, drift correction, and pulse sequencing. Furthermore, TRACS offers fast inference and robust generalization across diverse experimental conditions and device architectures, also due to its end-to-end learning paradigm^{40,41}. In end-to-end learning approaches, a single trainable model maps inputs to outputs without intermediate stages.

We evaluate TRACS' performance on triple point and charge transition detection, using experimental data acquired from three different quantum devices: an accumulation-mode Si/SiGe device⁴², a depletion-mode Ge/SiGe heterostructure⁴³, and an accumulation-mode Ge/SiGe heterostructure^{44,45}. Notably, TRACS exhibits strong performance and outperforms a popular CNN object detection architecture⁴⁶, achieving a median error in

^{a)}Shared first authorship

^{b)}Corresponding author: pranav.vaidhyanathan@stcatz.ox.ac.uk

^{c)}Corresponding author: natalia.ares@eng.ox.ac.uk

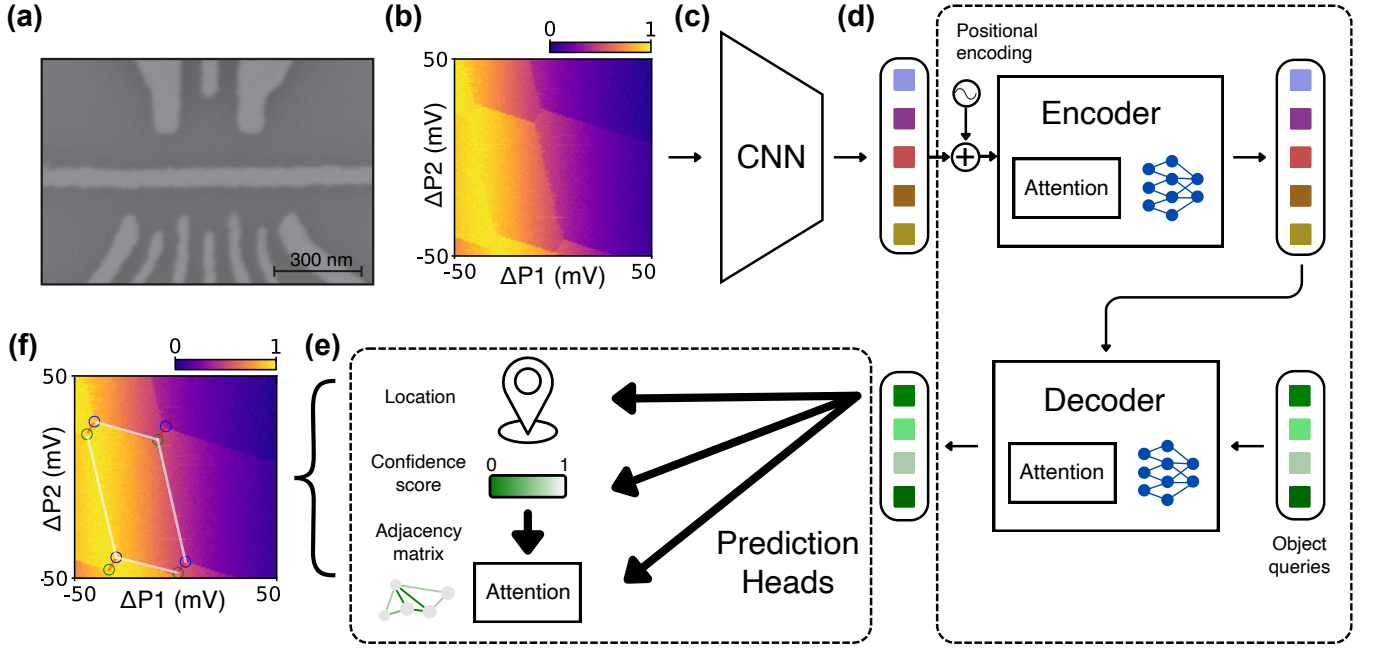


FIG. 1. **Overview of TRACS' architecture.** (a) Micrograph of a depletion-mode Ge/SiGe device similar to the one used in this work (Device B). (b) Example of a (simulated) charge stability diagram that can be fed as an input to TRACS. (c) The first stage of TRACS is a convolutional neural network. After a linear mapping, the resulting pixel feature vectors serve as tokens. Tokens are enriched with positional encoding and fed into the encoder of a transformer (d). Its output and a set of learnable object queries form the input to a transformer decoder. Both encoder and decoder use the attention mechanism and multilayer perceptrons as fundamental building blocks. (e) Prediction heads “interpret” the decoder’s outputs and return confidence scores on whether an instance is a triple point pair, their location, and their connectivity. (f) The original charge stability diagram used as an input [from (b)] is returned, overlaid with the final transformer output.

placement of triple point coordinates within 3% of the voltage scan range while remaining agnostic to device materials and gate architectures. Our work thus opens the door to more robust, general, and scalable strategies for autonomous quantum dot tuning, characterization, and control.

II. METHODS

Our algorithm, TRACS, builds on the powerful object detection transformer (DETR)⁴⁷, and processes the input CSD through a convolutional neural network, followed by a transformer, and finally a set of prediction heads. While CNNs excel at local feature extraction, demonstrate robustness to pixel noise, and exhibit translational invariance, they are limited in their ability to assimilate information across those local features. Transformers¹, on the other hand, are powerful sequence-to-sequence models that can reason across all elements in a sequence, or all local features, via the attention mechanism. The attention mechanism models pairwise relations between all elements (or so-called tokens) in a dynamic manner via learned parameters. The final prediction heads map the outputs of the transformer to the final outputs. These are the locations of the triple points, their confidence scores, and an adjacency matrix for their connectivity (i.e., trac-

ing of the charge transitions). The novel prediction head for connectivity is based on the attention mechanism¹.

The pipeline of TRACS is schematized in Fig. 1. The model inputs are charge sensed charge stability diagrams acquired by measuring the current or rf voltage output of a proximal charge sensor, while sweeping two gate voltages of a quantum dot device.⁴⁸ The resulting image, with a single scalar value per pixel (channel dimension 1), is normalized to the range [0, 1] and provided to TRACS as input. This image is then passed through a convolutional neural network. The core building blocks of CNNs are learnable filters, that are convolved with the image, and pooling layers, which downsample the input while increasing channel dimension. A linear layer is applied to each pixel of the CNN output to generate tokens, which serve as input to the transformer encoder. These tokens are high-dimensional vector representations, over which the attention mechanism operates to model pairwise relationships. Positional encoding is added to the tokens to retain spatial information since the transformer architecture is permutation-invariant. Several attention layers between the tokens (self-attention), as well as multi-layer perceptrons, transform the input tokens of the encoder into tokens with an enriched feature representation. This encoder output is fed into the transformer decoder along with a set of learnable tokens called object queries, which can be thought of as empty slots for triple point instances.

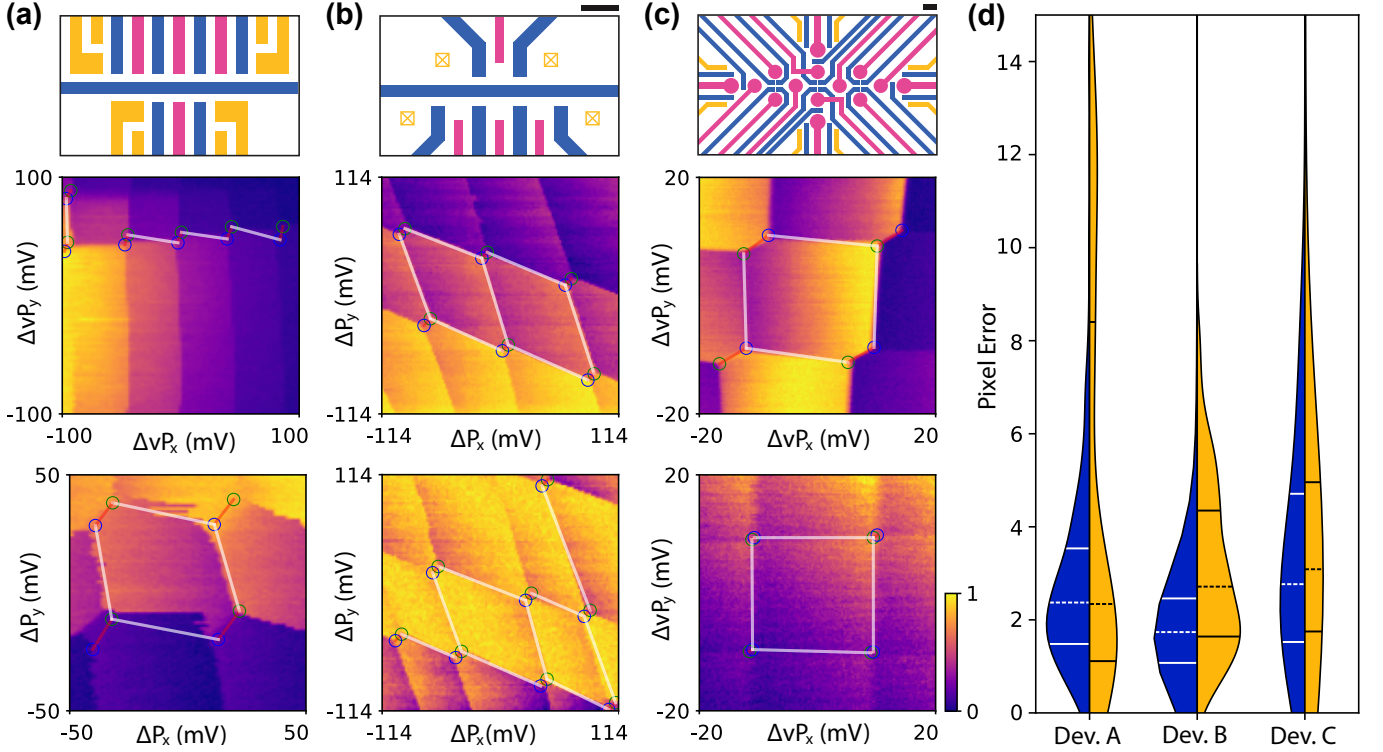


FIG. 2. **Device schematics, example outputs, and triple point location performance of TRACS.** (a)–(c) Schematics of the devices used in this work, accompanied by two CSDs and the output of TRACS overlaid; (a) Device A: an accumulation-mode electron device on a Si/SiGe heterostructure, (b) Device B: a depletion-mode hole device on a Ge/SiGe heterostructure, (c) Device C: an accumulation-mode hole device on a Ge/SiGe heterostructure. Pink, blue and yellow layers correspond to plunger, barrier and accumulation (or ohmic) gates (or reservoirs), respectively. Additional screening layers have been omitted for clarity. The scale bar in each panel corresponds to 100nm, see Ref.⁴² for details on Device A. $P_{\{x,y\}}$ corresponds to a plunger gate and $vP_{\{x,y\}}$ corresponds to a virtualized plunger gate. (d) Violin plots of the error in triple point locations, measured as a pixel distance, of TRACS (blue) and YOLO (yellow). Dashed lines indicate median errors and solid lines separate lower and upper quartiles. 10 pixels correspond to $10/128 \sim 8\%$ of the mV range for a CSD, see Appendix A.

The decoder uses a combination of cross-attention, self-attention on the object queries, and multi-layer perceptrons, to yield the final output tokens. Cross-attention contextualizes the relationship between encoder output tokens and object queries.

Each output token represents a potential triple point instance as a high-dimensional vector. Three prediction heads map the tokens to the final outputs. The first head yields a pair of confidence scores, distinguishing a pair of triple points (both values close to 1) from no pair (both values close to 0) via a linear projection and sigmoid function. The second head outputs four values corresponding to the x and y coordinates for a pair of triple points via a linear projection and clamping. The third head consists of two layers of attention and multi-layer perceptrons and outputs an adjacency matrix of shape $(n_{\text{obj}}, n_{\text{obj}}, 3)$. Here, n_{obj} is the number of output tokens and the three values at index $[i, j, :]$ correspond to “probabilities”. The first “probability” indicates whether no line is present between token i and token j , the second that the upper triple point of token i is connected with token j , and the third that the lower triple point of token i is connected with token j . Since upper triple

points can only be connected to lower triple points, the matrix elements corresponding to the same connection are averaged.

TRACS is trained in a supervised manner via gradient-based optimization of the loss function

$$\mathcal{L}_{\text{total}} = \mathcal{L}_{\text{BCE}}^{\text{con}} + \mathcal{L}_{\text{wing}}^{\text{loc}} + \mathcal{L}_{\text{focal}}^{\text{adj}}. \quad (1)$$

The binary cross-entropy loss $\mathcal{L}_{\text{BCE}}^{\text{con}}$ penalizes wrong confidence scores. The wing loss⁴⁹ $\mathcal{L}_{\text{wing}}^{\text{loc}}$ penalizes incorrect triple point locations and is more effective for computer vision localization tasks than standard Euclidean distance. The focal loss⁵⁰ $\mathcal{L}_{\text{focal}}^{\text{adj}}$ acts on the adjacency matrix, down-weights the contributions of well-classified examples, and takes class imbalance into account. Each of these terms is formally defined in Appendix A.

The set of predicted triple point pairs and the ground truth set are both unordered. However, an efficient bijective matching can be computed to minimize $\mathcal{L}_{\text{BCE}}^{\text{con}} + \mathcal{L}_{\text{wing}}^{\text{loc}}$. In practice, we normalize and weight the different terms of $\mathcal{L}_{\text{total}}$ as well as use regularization. See Appendix A for further details, and the original DETR publication⁴⁷ for background.

The TRACS model is trained on 500,000 charge stability diagrams generated together with ground truth labels using QArray^{51,52}. This GPU-accelerated simulator computes ground-state charge configurations of quantum dot arrays using a constant capacitance model. For closer resemblance with experimental CSDs, thermal broadening, white noise, telegraph noise and latching are included in the training data, which is supported by QArray. Simulation parameters are sampled from uniform distributions, with bounds selected to span a wide range of experimental conditions, see the Data Availability.

Although TRACS is deliberately restricted to simulated-data training in this work, its transformer architecture supports a two-stage training paradigm^{53–55}. In the first stage, the model undergoes pre-training on large amount of simulated data; in the second, it is “fine-tuned” on a smaller set of experimental data.

III. RESULTS

We test our model on CSDs acquired from three different device architectures. These are shown schematically in Fig. 2(a)–(c). Device A is an accumulation-mode electron device on a Si/SiGe heterostructure, Device B is a depletion-mode hole device on a Ge/SiGe heterostructure, and Device C is an accumulation-mode hole device on a Ge/SiGe heterostructure. Refer to Appendix B for details on the measurement set-up and to Appendix C for test set sizes. For each device, two examples of CSDs are presented together with the output of TRACS. TRACS is capable of identifying triple points and their connections with high accuracy across CSDs with different noise characteristics and varying numbers of triple points. In particular, in panel (a), we showcase TRACS’ capabilities on highly latched and non-centered data which, a pixel classification-based method typically fails to handle effectively. In panel (c), we highlight TRACS’ capacity to operate on (over-) virtualized data, enabling verification of the virtualization process and supporting subsequent tuning steps.

We benchmark TRACS against a fully CNN-based model – the **Y**ou **O**nly **L**ook **O**nce (YOLO) architecture⁴⁶ – keeping the CNN from the first stage of TRACS. YOLOv1 was chosen for its efficiency, simplicity, and proven effectiveness in real-time object detection tasks. However, it does not allow for line detection, without significant modification to the original architecture. Training and test data remain the same.

The first four rows of Table I report the recall and precision of TRACS and YOLO for triple point detection on test sets from all three devices, as well as a test set of simulated CSDs. Recall and precision formalize the notion of the “percentage of correct predictions” and are defined by $TP/(TP + FN)$ and $TP/(TP + FP)$. TP denotes the number of true positive predictions, FN the number of false negative predictions, and FP the number of false positive predictions. For all benchmarks, we use a clas-

TABLE I. Model evaluation and benchmark of TRACS (our model) vs. YOLOv1 (CNN-based model) on point detection (PD). Line Detection (LD) results are reported for TRACS only, since YOLO is not suited for this task. The results include median slope error of TRACS corresponding to capacitive values for experimental data from three different device architectures as well as simulated test set.

	Dev A	Dev B	Dev C	Simul
PD TRACS Recall	0.87	0.84	0.90	0.98
PD YOLOv1 Recall	0.84	0.77	0.76	0.92
PD TRACS Precision	0.93	0.94	0.92	0.94
PD YOLOv1 Precision	0.86	0.95	0.85	0.94
LD TRACS Recall	0.95	0.95	0.91	0.98
LD YOLOv1 Recall	– ^a	– ^a	– ^a	– ^a
LD TRACS Precision	0.93	0.85	0.94	0.94
LD YOLOv1 Precision	– ^a	– ^a	– ^a	– ^a
Median slope error	0.031	0.039	0.015	0.022

^a Original YOLOv1 architecture cannot predict line connectivity.

sification threshold of 0.5, i.e. confidence scores above this threshold are classified as triple points. Increasing the threshold improves precision, but reduces recall. A ground truth triple point is considered correctly detected if the predicted location is within 15 image pixels of the actual position, see Appendix A for details. TRACS outperforms YOLO on the simulated test set and generalizes significantly better to quantum device data with an improvement of more than 5 percentage points on average for recall and precision. This corresponds to a 45% reduction in false negatives (missed triple points) and a 19% reduction in false positives.

The distribution of error in triple point locations is shown in Fig. 2(d). This is only well defined and reported for all true positive triple points, hence, the blue and yellow areas are not equal in size. For all devices, TRACS outperforms YOLO, as evidenced by its lower third-quartile bar.

Rows five to eight of Table I report recall and precision for all connections between true positive triple points. Here, TRACS once again generalizes well to experimental CSDs with high accuracy.

From the connectivity, calculating the slope of lines between triple points becomes trivial. Slopes correspond to the strength of capacitive coupling between the gates swept in a CSD and are important quantities for their virtualization. We report a median slope error in Table 1.

With TRACS, point and line detection is performed in a single forward pass through the model. On an Intel core i7 CPU, we measure an average inference time of 83ms and expect faster inference on a GPU. This is 1-3 orders of magnitude faster than inference times reported in previous work³².

IV. CONCLUSION & OUTLOOK

In this work, we introduced TRACS for the end-to-end analysis of charge stability diagrams with transformers. TRACS automatically detects triple points in CSDs and infers their connectivity, crucial information for automated device tuning procedures, in particular for gate virtualization, navigating to charge states, and pulse sequencing. With inference in tens of milliseconds, TRACS can also be woven into closed-loop control algorithms for charge-offset drift correction. TRACS generalizes well from simulated data to a wide range of measured CSDs, as evidenced by its strong performance across three different device architectures, including SiGe-based devices operating both in depletion and accumulation modes.

It is also important to note that, instead of relying on specific tuning procedures, TRACS abstracts charge stability diagrams into connectivity graphs of triple points. This abstraction makes it possible to apply the same control routines across different device architectures, multi-dot arrays, and material platforms, without redesigning the underlying tuning logic.

TRACS lays the groundwork for a new generation of tuning algorithms. Next steps include the integration of more advanced experiment planners and protocols. We anticipate that our approach will become a core component of next-generation quantum dot control systems, dramatically accelerating device characterization, tuning, and ultimately the deployment of large-scale quantum processors.

ACKNOWLEDGMENTS

The authors would like to thank Jaime Saez-Mollejo and Georgios Katsaros for the fabrication and measurement of Device B. The authors would also like to thank the authors of reference³² for making their device data openly available. N.A. acknowledges support from the European Research Council (grant agreement 948932), the Royal Society (URF-R1-191150), Innovate UK project AutoQT (grant number 1004359) and the United States Army Research Office under Award No. W911NF-24-2-0043. Views and opinions expressed are however those of the authors only and do not necessarily reflect those of the European Union, Research Executive Agency or UK Research & Innovation. Neither the European Union nor UK Research & Innovation can be held responsible for them. P.V. is supported by the United States Army Research Office under Award No. W911NF-21-S-0009-2. L.S. and C.C. acknowledge support from the UKRI Doctoral Training Partnership related to EP/W524311/1 (project refs. 2886876 and 2887634).

AUTHOR DECLARATIONS

Conflict of Interest

Natalia Ares declares a competing interest as a founder of QuantrolOx, which develops machine learning-based software for quantum control. All remaining authors declare no conflicts of interest.

Author Contributions

Rahul Marchand: Software (lead); Data curation (lead); Formal analysis (lead); Methodology (lead). **Lucas Schorling:** Writing – original draft (lead); Visualization (lead); Supervision (equal); Methodology (equal). **Cornelius Carlsson:** Conceptualization (equal), Investigation (equal), Writing – review & editing (equal); Visualization (equal); Methodology (supporting). **Jonas Schuff:** Conceptualization (equal); Methodology (equal); Investigation (supporting). **Barnaby van Straaten:** Investigation (equal); Software (supporting). **Taylor L. Patti:** Methodology (supporting); Software (supporting). **Federico Fedele:** Writing – review & editing (equal). **Joshua Ziegler:** Investigation (equal). **Parth Girdhar:** Supervision (supporting). **Pranav Vaidhyanathan:** Supervision (equal); Methodology (equal); Writing – review & editing (equal). **Natalia Ares:** Funding acquisition (lead); Supervision (equal); Writing – review & editing (equal).

DATA AVAILABILITY

All test data and the software code, including files to generate the training data, will be made public upon final publication.

Appendix A: Details of TRACS

TRACS is trained on CSDs with a 128×128 pixel resolution. During inference, CSDs with other resolutions are linearly rescaled to match the expected dimensions. Therefore, for a specific CSD, the pixel error can be converted to millivolts (mV) by dividing it by 128 and multiplying by the CSD’s voltage range in mV.

The architecture of the convolutional neural network and its parameters are similar to ResNet-18⁵⁶, adapted to handle greyscale images, and work with lower image resolutions than those in the ImageNet dataset. The first layer of filters fed to the transformer expects a channel dimension of 1, hence pooling layers as well as the final averaging and fully connected layer of ResNet-18 were removed, and strides were decreased. The modified ResNet-18 outputs 16×16 pixels with a channel width of 512. This is mapped to the transformer input of 256

tokens of dimension 128 via a convolution with kernel size 1. The transformer encoder and decoder consist of 4 layers with 8 attention heads and have a dropout of 0.1 and a feedforward dimension of 2048.

The inputs to the connectivity prediction head are the decoder output tokens and the corresponding two confidence scores. Those confidence scores and tokens are concatenated and linearly projected to dimension 128. Those are fed into a transformer encoder architecture with 2 layers and 1 attention head.

For every CSD, we have a set of labels for pairs of triple points consisting of confidence scores $c_{i,p} \in \mathbb{R}$, locations $x_{i,p} \in \mathbb{R}^2$, where i and j refer to the instances of triple point pairs and $p = 1, 2$ refers to each point in the pair individually. Furthermore, we have three values $a_{ij,m} \in \mathbb{R}$ for the connectivity between instance i and instance j for $m = 1, 2, 3$.

The TRACS predictions are given by $\hat{c}_{i,p}$, $\hat{x}_{i,p}$, and $\hat{a}_{ij,m}$. The total loss function can be written as

$$\begin{aligned} \mathcal{L}_{\text{total}} &= \mathcal{L}_{\text{BCE}}^{\text{con}} + \mathcal{L}_{\text{wing}}^{\text{loc}} + \mathcal{L}_{\text{focal}}^{\text{adj}} \\ &= \alpha_1 \sum_{i=1}^{n_q} \sum_{p=1,2} -c_i \log(\hat{c}_{\sigma(i)}) - \beta_1(1 - c_i) \\ &\quad \log(1 - \hat{c}_{\sigma(i)}) \\ &\quad + \alpha_2 \sum_{i=1}^{n_q} \sum_{p=1,2} \mathcal{L}_{\text{wing}}(x_i, \hat{x}_{\sigma(i)}) \\ &\quad + \alpha_3 \sum_{\substack{i,j=1 \\ c_i=1 \\ c_j=1}}^{n_q, n_q} \sum_{m=1,2,3} w_m l_{\sigma(i)\sigma(j),m} (1 - \hat{l}_{\sigma(i)\sigma(j),m})^\gamma \\ &\quad \log(\hat{l}_{\sigma(i)\sigma(j),m}), \end{aligned} \quad (\text{A1})$$

where $\alpha_1 = 1, \alpha_2 = 0.05, \alpha_3 = 0.5$ weight the different loss terms, $n_q = 25$ is the number of object queries, $\beta_1 = 0.5$, $w_1 = 0.3, w_2 = w_3 = 1$ are weights to counteract class imbalance, and $\gamma = 2$. $\sigma(i)$ represents the permutation of labels and object tokens based on the minimal cost matching via the Hungarian algorithm. The double subscripts $c_i = 1$ indicate that the sum only includes terms fulfilling this condition. $\mathcal{L}_{\text{wing}}$ has width $\omega = 0.05$ and curvature $\epsilon = 0.01$.

We use the AdamW optimizer with a learning rate of $2e-5$, a learning rate scheduler, weight decay of 0.0001, batch size of 256 and train for 225 epochs.

Appendix B: Experimental Set-up

All data presented in this paper was acquired via charge sensing with a proximal single electron/hole transistor (SET/SHT) tuned to the flank of a Coulomb peak. Measurements are acquired in dilution refrigeration units at base temperatures below 100 mK. In the case of Devices B and C, read-out was done by reflecting a mi-

crowave tone off an SHT ohmic in the range 100-250 MHz. The signal couples to the device through an LC matching network on the sample PCB, making the reflected signal sensitive to impedance changes caused by fluctuations in the device's hole occupancy⁴⁸. The reflected signal is routed to a demodulation circuit at room temperature via a directional coupler mounted inside the cryogenic set-up. In the case of Device A, read-out is achieved through direct amplification of the sensor's current using a dual-stage SiGe heterojunction bipolar transistor (HBT), located on the sample PCB⁵⁷, which is further amplified at room temperature. The SET's source contact is DC biased through the junction's emitter, and coupled to an AC signal applied on the SET's drain at around 100 kHz. For further details on individual set-ups and fabrication, refer to⁴²⁻⁴⁴ for devices A, B, and C, respectively.

Appendix C: Further details for results

The three test sets corresponding to devices A, B, and C contain 67, 72, and 60 CSDs, respectively. The simulated test set includes 128 CSDs.

- ¹A. Vaswani, N. Shazeer, N. Parmar, J. Uszkoreit, L. Jones, A. N. Gomez, L. Kaiser, and I. Polosukhin, "Attention is all you need," *Advances in neural information processing systems* **30** (2017).
- ²L. C. Melo, "Transformers are meta-reinforcement learners," in *international conference on machine learning* (PMLR, 2022) pp. 15340–15359.
- ³T. Lin, Y. Wang, X. Liu, and X. Qiu, "A survey of transformers," *AI open* **3**, 111–132 (2022).
- ⁴A. Dosovitskiy, L. Beyer, A. Kolesnikov, D. Weissenborn, X. Zhai, T. Unterthiner, M. Dehghani, M. Minderer, G. Heigold, S. Gelly, J. Uszkoreit, and N. Houlsby, "An image is worth 16x16 words: Transformers for image recognition at scale," (2021), arXiv:2010.11929 [cs.CV].
- ⁵Y. Zhou, U. Alon, X. Chen, X. Wang, R. Agarwal, and D. Zhou, "Transformers can achieve length generalization but not robustly," (2024), arXiv:2402.09371 [cs.LG].
- ⁶I. Goodfellow, Y. Bengio, and A. Courville, *Deep Learning* (MIT Press, 2016) book in preparation for MIT Press.
- ⁷U. Kamath, K. Graham, and W. Emara, *Transformers for machine learning: a deep dive* (Chapman and Hall/CRC, 2022).
- ⁸G. Whittle, J. Ziomek, J. Rawling, and M. A. Osborne, "Distribution transformers: Fast approximate bayesian inference with on-the-fly prior adaptation," arXiv preprint arXiv:2502.02463 (2025).
- ⁹R. Roy and H. M. Al-Hashimi, "Alphafold3 takes a step toward decoding molecular behavior and biological computation," *Nature Structural & Molecular Biology* **31**, 997–1000 (2024).
- ¹⁰N. Sanghai and N. B. Brown, "Advances in transformers for robotic applications: A review," (2024), arXiv:2412.10599 [cs.RO].
- ¹¹P. Vaidhyanathan, F. Marquardt, M. T. Mitchison, and N. Ares, "Quantum feedback control with a transformer neural network architecture," (2024), arXiv:2411.19253 [quant-ph].
- ¹²X. Xue, M. Russ, N. Samkharadze, B. Undseth, A. Sammak, G. Scappucci, and L. M. K. Vandersypen, "Quantum logic with spin qubits crossing the surface code threshold," *Nature* **601**, 343–347 (2022).
- ¹³A. Noiri, K. Takeda, T. Nakajima, T. Kobayashi, A. Sammak, G. Scappucci, and S. Tarucha, "Fast universal quantum gate above the fault-tolerance threshold in silicon," *Nature* **601**, 338–342 (2022).

- ¹⁴J. Y. Huang, R. Y. Su, W. H. Lim, M. Feng, B. van Straaten, B. Severin, W. Gilbert, N. Dumoulin Stuyck, T. Tanttu, S. Serano, J. D. Cifuentes, I. Hansen, A. E. Seedhouse, E. Vahapoglu, R. C. C. Leon, N. V. Abrosimov, H.-J. Pohl, M. L. W. Thewalt, F. E. Hudson, C. C. Escott, N. Ares, S. D. Bartlett, A. Morello, A. Saraiva, A. Laucht, A. S. Dzurak, and C. H. Yang, “High-fidelity spin qubit operation and algorithmic initialization above 1 k,” *Nature* **627**, 772–777 (2024).
- ¹⁵L. C. Camenzind, S. Geyer, A. Fuhrer, R. J. Warburton, D. M. Zumbühl, and A. V. Kuhlmann, “A hole spin qubit in a fin field-effect transistor above 4 kelvin,” *Nature Electronics* **5**, 178–183 (2022).
- ¹⁶S. Neyens, O. K. Zietz, T. F. Watson, F. Luthi, A. Nethwewala, H. C. George, E. Henry, M. Islam, A. J. Wagner, F. Borjans, *et al.*, “Probing single electrons across 300-mm spin qubit wafers,” *Nature* **629**, 80–85 (2024).
- ¹⁷A. Zwerwer, T. Krähenmann, T. Watson, L. Lampert, H. C. George, R. Pillarisetty, S. Bojarski, P. Amin, S. Amitonov, J. Boter, *et al.*, “Qubits made by advanced semiconductor manufacturing,” *Nature Electronics* **5**, 184–190 (2022).
- ¹⁸G. Burkard, T. D. Ladd, A. Pan, J. M. Nichol, and J. R. Petta, “Semiconductor spin qubits,” *Reviews of Modern Physics* **95**, 025003 (2023).
- ¹⁹F. Fedele, A. Chatterjee, S. Fallahi, G. C. Gardner, M. J. Manfra, and F. Kuemmeth, “Simultaneous operations in a two-dimensional array of singlet-triplet qubits,” *PRX Quantum* **2**, 040306 (2021).
- ²⁰S. G. Philips, M. T. Mądzik, S. V. Amitonov, S. L. de Snoo, M. Russ, N. Kalhor, C. Volk, W. I. Lawrie, D. Brousse, L. Tryputen, B. Paquelet Wuetzm, A. Sammak, G. Scappucci, and L. M. Vandersypen, “Universal control of a six-qubit quantum processor in silicon,” *Nature* **609**, 919–924 (2022).
- ²¹N. Ares, “Machine learning as an enabler of qubit scalability,” *Nature Reviews Materials* **6**, 870–871 (2021).
- ²²Y. Alexeev, M. H. Farag, T. L. Patti, M. E. Wolf, N. Ares, A. Aspuru-Guzik, S. C. Benjamin, Z. Cai, Z. Chandani, F. Fedele, N. Harrigan, J.-S. Kim, E. Kyoseva, J. G. Lietz, T. Lubowe, A. McCaskey, R. G. Melko, K. Nakaji, A. Peruzzo, S. Stanwyck, N. M. Tubman, H. Wang, and T. Costa, “Artificial intelligence for quantum computing,” (2024), arXiv:2411.09131 [quant-ph].
- ²³B. Severin, D. T. Lennon, L. C. Camenzind, F. Vigneau, F. Fedele, D. Jirovec, A. Ballabio, D. Chrastina, G. Isella, M. de Kruijff, M. J. Carballido, S. Svab, A. V. Kuhlmann, S. Geyer, F. N. M. Froning, H. Moon, M. A. Osborne, D. Sejdinovic, G. Katsaros, D. M. Zumbühl, G. A. D. Briggs, and N. Ares, “Cross-architecture tuning of silicon and sige-based quantum devices using machine learning,” *Scientific Reports* **14** (2024), 10.1038/s41598-024-67787-z.
- ²⁴D. L. Craig, H. Moon, F. Fedele, D. T. Lennon, B. van Straaten, F. Vigneau, L. C. Camenzind, D. M. Zumbühl, G. A. D. Briggs, M. A. Osborne, D. Sejdinovic, and N. Ares, “Bridging the reality gap in quantum devices with physics-aware machine learning,” *Phys. Rev. X* **14**, 011001 (2024).
- ²⁵B. van Straaten, F. Fedele, F. Vigneau, J. Hickie, D. Jirovec, A. Ballabio, D. Chrastina, G. Isella, G. Katsaros, and N. Ares, “All rf-based tuning algorithm for quantum devices using machine learning,” (2022), arXiv:2211.04504 [cond-mat.mes-hall].
- ²⁶V. Nguyen, S. B. Orbell, D. T. Lennon, H. Moon, F. Vigneau, L. C. Camenzind, L. Yu, D. M. Zumbühl, G. A. D. Briggs, M. A. Osborne, D. Sejdinovic, and N. Ares, “Deep reinforcement learning for efficient measurement of quantum devices,” *npj Quantum Information* **7** (2021), 10.1038/s41534-021-00434-x.
- ²⁷J. Hickie, B. van Straaten, F. Fedele, D. Jirovec, A. Ballabio, D. Chrastina, G. Isella, G. Katsaros, and N. Ares, “Automated long-range compensation of an rf quantum dot sensor,” *Phys. Rev. Appl.* **22**, 064026 (2024).
- ²⁸J. Schuff, D. T. Lennon, S. Geyer, D. L. Craig, F. Fedele, F. Vigneau, L. C. Camenzind, A. V. Kuhlmann, G. A. D. Briggs, D. M. Zumbühl, D. Sejdinovic, and N. Ares, “Identifying pauli spin blockade using deep learning,” *Quantum* **7**, 1077 (2023), arXiv:2202.00574v4.
- ²⁹L. Schorling, P. Vaidhyathan, J. Schuff, M. J. Carballido, D. Zumbühl, G. Milburn, F. Marquardt, J. Foerster, M. A. Osborne, and N. Ares, “Meta-learning characteristics and dynamics of quantum systems,” (2025), arXiv:2503.10492 [quant-ph].
- ³⁰J. Schuff, M. J. Carballido, M. Kotzagiannidis, J. C. Calvo, M. Caselli, J. Rawling, D. L. Craig, B. van Straaten, B. Severin, F. Fedele, S. Svab, P. C. Kwon, R. S. Eggli, T. Patlatiuk, N. Korda, D. Zumbühl, and N. Ares, “Fully autonomous tuning of a spin qubit,” (2024), arXiv:2402.03931 [cond-mat.mes-hall].
- ³¹C. Carlsson, J. Saez-Mollejo, F. Fedele, S. Calcaterra, D. Chrastina, G. Isella, G. Katsaros, and N. Ares, “Automated all-rf tuning for spin qubit readout and control,” (2025), arXiv:2506.10834 [cond-mat.mes-hall].
- ³²A. S. Rao, D. Buterakos, B. van Straaten, V. John, C. X. Yu, S. D. Oosterhout, L. Stehouwer, G. Scappucci, M. Veldhorst, F. Borsoi, and J. P. Zwolak, “Mavis: Modular autonomous virtualization system for two-dimensional semiconductor quantum dot arrays,” (2024), arXiv:2411.12516 [cond-mat.mes-hall].
- ³³J. Ziegler, F. Luthi, M. Ramsey, F. Borjans, G. Zheng, and J. P. Zwolak, “Automated extraction of capacitive coupling for quantum dot systems,” *Phys. Rev. Appl.* **19**, 054077 (2023).
- ³⁴A. R. Mills, M. M. Feldman, C. Monical, P. J. Lewis, K. W. Larson, A. M. Mounce, and J. R. Petta, “Computer-automated tuning procedures for semiconductor quantum dot arrays,” *Applied Physics Letters* **115** (2019), 10.1063/1.5121444.
- ³⁵A. Chatterjee, F. Ansaloni, T. Rasmussen, B. Brovang, F. Fedele, H. Bohuslavskyi, O. Krause, and F. Kuemmeth, “Autonomous estimation of high-dimensional coulomb diamonds from sparse measurements,” *Physical Review Applied* **18** (2022), 10.1103/physrevapplied.18.064040.
- ³⁶R. Durrer, B. Kratochwil, J. Koski, A. Landig, C. Reichl, W. Wegscheider, T. Ihn, and E. Greplova, “Automated tuning of double quantum dots into specific charge states using neural networks,” *Physical Review Applied* **13** (2020), 10.1103/physrevapplied.13.054019.
- ³⁷J. P. Zwolak, T. McJunkin, S. S. Kalantre, S. F. Neyens, E. MacQuarrie, M. A. Eriksson, and J. M. Taylor, “Ray-based framework for state identification in quantum dot devices,” *PRX Quantum* **2**, 020335 (2021).
- ³⁸F. Hader, F. Fuchs, S. Fleitmann, *et al.*, “Automated charge transition detection in quantum dot charge stability diagrams,” *TechRxiv* (2024), 10.36227/techrxiv.172963185.53119182/v1, doi:10.36227/techrxiv.172963185.53119182/v1.
- ³⁹W. Wang, J. D. Rooney, and H. Jiang, “Efficient characterization of a double quantum dot using the hubbard model,” *Journal of Applied Physics* **136** (2024).
- ⁴⁰B. Wilder, E. Ewing, B. Dilkina, and M. Tambe, “End to end learning and optimization on graphs,” *Advances in Neural Information Processing Systems* **32** (2019).
- ⁴¹T. Glasmachers, “Limits of end-to-end learning,” in *Asian conference on machine learning* (PMLR, 2017) pp. 17–32.
- ⁴²H. C. George, M. T. Mądzik, E. M. Henry, A. J. Wagner, M. M. Islam, F. Borjans, E. J. Connors, J. Corrigan, M. Curry, M. K. Harper, *et al.*, “12-spin-qubit arrays fabricated on a 300 mm semiconductor manufacturing line,” *Nano Letters* **25**, 793–799 (2024).
- ⁴³J. Saez-Mollejo, D. Jirovec, Y. Schell, J. Kukucka, S. Calcaterra, D. Chrastina, G. Isella, M. Rimbach-Russ, S. Bosco, and G. Katsaros, “Microwave driven singlet-triplet qubits enabled by site-dependent g-tensors,” arXiv preprint arXiv:2408.03224 (2024).
- ⁴⁴V. John, C. X. Yu, B. van Straaten, E. A. Rodríguez-Mena, M. Rodríguez, S. Oosterhout, L. E. Stehouwer, G. Scappucci, S. Bosco, M. Rimbach-Russ, *et al.*, “A two-dimensional 10-qubit array in germanium with robust and localised qubit control,” arXiv preprint arXiv:2412.16044 (2024).
- ⁴⁵L. E. A. Stehouwer, C. X. Yu, B. van Straaten, A. Tosato, V. John, D. D. Esposti, A. Elsayed, D. Costa, S. D. Oosterhout, N. W. Hendrickx, M. Veldhorst, F. Borsoi, and G. Scappucci, “Exploiting epitaxial strained germanium for scaling low

- noise spin qubits at the micron-scale,” (2025), arXiv:2411.11526 [cond-mat.mes-hall].
- ⁴⁶J. Redmon, S. Divvala, R. Girshick, and A. Farhadi, “You only look once: Unified, real-time object detection,” in *Proceedings of the IEEE conference on computer vision and pattern recognition* (2016) pp. 779–788.
- ⁴⁷N. Carion, F. Massa, G. Synnaeve, N. Usunier, A. Kirillov, and S. Zagoruyko, “End-to-end object detection with transformers,” in *European conference on computer vision* (Springer, 2020) pp. 213–229.
- ⁴⁸F. Vigneau, F. Fedele, A. Chatterjee, D. Reilly, F. Kuemmeth, M. F. Gonzalez-Zalba, E. Laird, and N. Ares, “Probing quantum devices with radio-frequency reflectometry,” *Applied Physics Reviews* **10** (2023).
- ⁴⁹Z.-H. Feng, J. Kittler, M. Awais, P. Huber, and X.-J. Wu, “Wing loss for robust facial landmark localisation with convolutional neural networks,” in *Proceedings of the IEEE conference on computer vision and pattern recognition* (2018) pp. 2235–2245.
- ⁵⁰T.-Y. Lin, P. Goyal, R. Girshick, K. He, and P. Dollár, “Focal loss for dense object detection,” (2018), arXiv:1708.02002 [cs.CV].
- ⁵¹B. van Straaten, J. Hickie, L. Schorling, J. Schuff, F. Fedele, and N. Ares, “Qarray: A gpu-accelerated constant capacitance model simulator for large quantum dot arrays,” *SciPost Physics Codebases*, 035 (2024).
- ⁵²B. van Straaten, J. Hickie, L. Schorling, J. Schuff, F. Fedele, and N. Ares, “Codebase release 1.3 for qarray,” *SciPost Physics Codebases*, 035 (2024).
- ⁵³J. Devlin, M.-W. Chang, K. Lee, and K. Toutanova, “Bert: Pre-training of deep bidirectional transformers for language understanding,” in *Proceedings of the 2019 conference of the North American chapter of the association for computational linguistics: human language technologies, volume 1 (long and short papers)* (2019) pp. 4171–4186.
- ⁵⁴E. J. Hu, Y. Shen, P. Wallis, Z. Allen-Zhu, Y. Li, S. Wang, L. Wang, W. Chen, *et al.*, “Lora: Low-rank adaptation of large language models,” *ICLR* **1**, 3 (2022).
- ⁵⁵I. E. Marouf, E. Tartaglione, and S. Lathuilière, “Mini but mighty: Finetuning vits with mini adapters,” in *Proceedings of the IEEE/CVF Winter Conference on Applications of Computer Vision* (2024) pp. 1732–1741.
- ⁵⁶K. He, X. Zhang, S. Ren, and J. Sun, “Deep residual learning for image recognition,” in *Proceedings of the IEEE conference on computer vision and pattern recognition* (2016) pp. 770–778.
- ⁵⁷M. J. Curry, T. D. England, N. Bishop, G. Ten-Eyck, J. R. Wendt, T. Pluym, M. Lilly, S. M. Carr, and M. S. Carroll, “Cryogenic preamplification of a single-electron-transistor using a silicon-germanium heterojunction-bipolar-transistor,” *Applied Physics Letters* **106** (2015).